micromachines

Article

Tunable Broadband Terahertz Metamaterial Absorber Based on Vanadium Dioxide and Graphene

Laifang Zheng [1,2], Rui Feng [2,*], Huanting Shi [2] and Xuanjing Li [2]

1 Department of Electrical Engineering, Taiyuan Institute of Technology, Taiyuan 030008, China; zhenglf@tit.edu.cn
2 China Key Laboratory of Micro/Nano Devices and Systems, Ministry of Education, North University of China, Taiyuan 030051, China; shi1826923@163.com (H.S.); 15534081671@163.com (X.L.)
* Correspondence: 20220068@nuc.edu.cn

Abstract: We propose a dynamically tunable ultra-broadband terahertz metamaterial absorber, which was based on graphene and vanadium oxide (VO_2) and numerically demonstrated. The excellent absorption bandwidth almost entirely greater than 90% was as wide as 6.35 THz from 2.30 to 8.65 THz under normal incidence. By changing the conductivity of VO_2 from 20 S/m to 3×10^5 S/m, the absorption intensity could be dynamically tuned from 6% to 99%. The physical mechanism of the ultra-wideband absorption is discussed based on the interference cancelation, impedance matching theory, and field distributions, and the influences of the structural parameters on absorption are also discussed. According to the symmetric configuration, the absorption spectra of the considered polarizations were very close to each other, resulting in a polarization-insensitive structure. Such a tunable ultra-broadband absorber may have promising potential in the applications of modulating, cloaking, switching, and imaging technology.

Keywords: graphene; metamaterial absorber; terahertz; tunable; vanadium dioxide

check for updates

Citation: Zheng, L.; Feng, R.; Shi, H.; Li, X. Tunable Broadband Terahertz Metamaterial Absorber Based on Vanadium Dioxide and Graphene. *Micromachines* **2023**, *14*, 1715. https://doi.org/10.3390/mi14091715

Academic Editors: Xiaoguang Zhao and Rui You

Received: 28 July 2023
Revised: 22 August 2023
Accepted: 25 August 2023
Published: 31 August 2023

1. Introduction

The terahertz (THz) wave, whose frequency ranges from 0.1 to 10 THz, has broad application prospects in medical imaging, stealth technology, security inspection, broadband communication, and so on [1–4]. High-performance devices are essential for effective terahertz wave manipulation in order to achieve these favorable applications. Metamaterial perfect absorbers (MPAs) play an important role in numerous devices owing to their distinctive advantage of ultra-thinness. Following the discovery of the perfect narrow-band microwave absorber by Landy et al. in 2008 [5], many researchers have put forward a variety of metamaterials based on the THz wave absorption device model and have studied its single-band [6], multiband [7], and broadband characteristics [8]. However, the reported MPAs with a metal/insulator/metal structure still have some problems, such as a limited frequency or wavelength, unadjustable absorption performance, and low absorption efficiency, which greatly limit their further practical application. Hence, achieving high-performance tunable ultra-broadband terahertz MPAs has become an important research direction of terahertz technology.

In order to solve the above problems, some new two-dimensional materials have become research breakthroughs. Recently, many MPAs have been proposed to broaden the absorption bandwidth and achieve dynamic tunable characteristics, based on graphene [9,10], MoS_2 [11,12], LCD [13], and black phosphate [14]. Although these have the advantage of a greater degree of freedom in dynamic tunability, they are difficult to design because of the complex structure of the cell and its array and the shortcomings of incident angle or polarization dependence. VO_2 is a kind of phase-change material, switching between insulation and metal phase states, and it can be controlled by external stimuli such as heat, with the phase transition time able to be completed in picoseconds. The conductivity difference of VO_2 between the insulator and metal phase is approximately three orders of magnitude in the THz range, which makes it promising to design innovative devices. Many MPAs with broadband and tunable absorption properties have been reported, based on VO_2 [15–17]. However, there are many problems to be overcome, including their complex structure, narrow bandwidth, and poor absorption effectiveness. Thus, it is worth further exploring a novel broadband terahertz absorber with tunable absorption, improved insensitivity to polarization, and simpler geometry. Graphene is a two-dimensional material that consists of carbon atoms arranged in a planar hexagonal lattice. The Fermi level of graphene can be continuously tuned to change its surface conductivity by chemically doping it or introducing an external bias voltage, thus giving the tunable properties of graphene-based metamaterial absorption structures [18–20]. Several multifunctional THz absorbers combining graphene and VO_2 have been proposed [21–23]. However, most terahertz metamaterial absorbers still have some problems, such as a low absorption efficiency, untunable absorption performance, and insensitivity to polarization, which greatly limit their further practical application. Therefore, achieving a high-performance tunable terahertz metamaterial absorber has become an important research direction in the field of terahertz waves.

Inspired by these earlier studies, we proposed a tunable broadband terahertz metamaterial absorber based on vanadium dioxide and graphene. The proposed absorber comprised a periodic array of VO_2 resonant rings, a graphene layer, an insulator layer, and a metal ground plane. When the VO_2 was in the metallic state, the bandwidth of the designed absorber was 6.35 THz (2.30–8.65 THz), and the rate of absorption was almost entirely greater than 90%. When the frequency was between 2.30 and 8.65 THz, by controlling the conductivity of VO_2 from 2×10 S/m to 3×10^5 S/m, the absorption peak could be continually tuned from 6% to 99%. Moreover, for both transverse and longitudinal electromagnetic waves, the proposed absorber had an insensitivity to the polarization angle, with considerable incident angle tolerance. In the field of terahertz absorbers, the proposed multifunctional absorber is anticipated to be employed extensively.

2. Structure Design and Method

Figure 1 depicts a 3D schematic diagram and the geometric parameters of the designed tunable ultra-broadband terahertz metamaterial absorber. The absorber consisted of four layers, including the Au bottom layer, the insulator layer, the graphene layer, and the VO_2 layer with a resonant splitting ring pattern. As illustrated in Figure 1, the optimized structural parameters of the absorber unit were Px = 20 µm and Py = 20 µm. The thickness T_2 and conductivity of the bottom gold layer were 0.2 µm and 4.09×10^7 S/m, respectively [24], and the bottom layer acted as a mirror to ensure the complete reflection of the illuminating terahertz wave, thereby suppressing transmission. The relative permittivity of the insulator layer was 1.96, and it was assumed to be lossless in the simulation [25], with a thickness T_1 of 9.5 µm. The graphene layer was a single layer, and its thickness was 0 µm. The top VO_2 layer was composed of a ring with a cross opening, and the thickness T_3 of the VO_2 layer was 0.16 µm. The optimized geometric parameters of the splitting ring were R_1 = 7 µm, R_2 = 9.5 µm, and g = 0.625 µm. In order to analyze the magnitude response of the designed absorber, the CST microwave studio was used to perform the numerical simulation. We utilized the finite difference time domain (FDTD) method to simulate the structure and obtain the corresponding reflection and transmission coefficients. The PEC-PMC boundary conditions were used in the x and y directions to simulate the infinite array for normal incidence, while the open boundary was considered along the z direction.

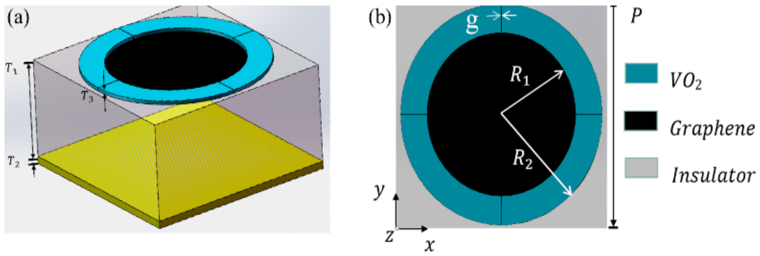

Figure 1. (**a**) 3D schematic of the ultra-broadband terahertz absorber unit cell. (**b**) Top view of the unit cell.

The interaction between electromagnetic waves and graphene can be explained by solving Maxwell's equation. All the calculations were carried out using the computer simulation technology (CST) microwave studio, and 3D numerical results were obtained. Since graphene was modeled as a material with a surface conductivity of σ_{gra} in the simulation, the surface conductivity of the graphene could be characterized using the following formulae (i.e., Kubo formula) [26]:

$$\sigma_{gra} = \sigma_{intra} + \sigma_{inter} \tag{1}$$

$$\sigma_{intra} = \frac{2e^2 k_B T}{\pi h^2} \frac{i}{\omega + i/\tau} \mathrm{In}[2\cos h(\frac{E_f}{2k_B T})] \tag{2}$$

$$\sigma_{inter} = \frac{e^2}{4h^2}[\frac{1}{2} + \frac{1}{\pi}\arctan(\frac{h\omega - 2E_f}{2}) \frac{i}{2\pi} \mathrm{In}\frac{(h\omega + 2E_f)^2}{(h\omega + 2E_f)^2 + 4(k_B T)^2}] \tag{3}$$

where e denotes the charge amount; h is the reduced Planck constant; k_B represents the Boltzmann constant; and T, τ, ω, and E_f are the ambient temperature (T = 294 K), the electron mobility, the incident light angular frequency, and the graphene Fermi level, respectively.

In accordance with the Pauli repulsion principle, the surface conductivity of the graphene was primarily derived by the intra-band conductivity, while the inter-band conductivity could be ignored. According to Refs. [27,28], Equation (1) can be simplified as:

$$\sigma_{gra} = \frac{e^2 E_f}{\pi h^2} \frac{i}{(\omega + i/\tau)} \tag{4}$$

It can be seen from Equation (4) that the surface conductivity of graphene is not only related to the angular frequency and relaxation time of the incident electromagnetic wave, but also to the Fermi level. Therefore, the surface conductivity of graphene can be adjusted by the relaxation time and the Fermi level. Both chemical doping and changing the bias voltage can be used in practice to attain a different Fermi level for graphene. In this work, the Fermi level E_f = 0 eV and carrier relaxation time τ = 0.1 ps were selected for broadband absorption.

In the terahertz range, the Drude model is adopted to describe the optical dielectric constant of VO_2 [29]:

$$\varepsilon(\omega)_{VO_2} = \varepsilon_\infty - \frac{\omega_p^2(\sigma)}{\omega^2 - i\gamma\omega} \tag{5}$$

where ε_∞, γ, and $\omega_p^2(\sigma)$ denote the high-frequency relative dielectric constant, the collision frequency, and the plasma frequency related to the conductivity, respectively. In this design, $\varepsilon_\infty = 9$, $\omega_p^2(\sigma) = \frac{\sigma}{\sigma_0}\omega_p^2(\sigma_0)$, $\sigma_0 = 3 \times 10^5$ S/m, $\omega_p^2(\sigma_0) = 1.45 \times 10^{15}$ rad/s, and $\gamma = 5.75 \times 10^{13}$ rad/s. As a kind of phase change material, the phase change process of VO_2 is accompanied by substantial alterations in the dielectric constant and electrical conductivity. Through external optical excitation [30], electrical excitation [31], or heating [32], VO_2 can be altered to a metallic state from an insulating state. Distinct dielectric constants are employed for various phase states during the VO_2 phase transition from insulator to metal. In the simulation, VO_2 was insulated, and we set the conductivity of VO_2 as $\sigma = 2 \times 10$ S/m in the normal temperature range. By the time the temperature rose to 68 °C, VO_2 transformed to the metallic state from the insulating state, and the electrical conductivity changed by four orders of magnitude as well. When VO_2 was in the metallic state, the VO_2 conductivity was set as $\sigma = 3 \times 10^5$ S/m. By substituting σ into Equation (5), the dielectric constant value of VO_2 was derived. At room temperature, VO_2 presented an insulating phase with a conductivity of 20 S/m. When the temperature reached the phase transition temperature, VO_2 was in the metallic phase, and the conductivity was 2×10^5 S/m.

Figure 2a,b show the evolution of the real part (Re(ε)) and imaginary part (Im(ε)) of the relative dielectric constant of VO_2 for different values of the conductivity, respectively. It is worth noting that Re(ε) varied from positive to negative with the increase in conductivity. When the state of VO_2 changed from the protective phase (20 S/m) to the metal phase (300,000 S/m), Im(ε) increased remarkably.

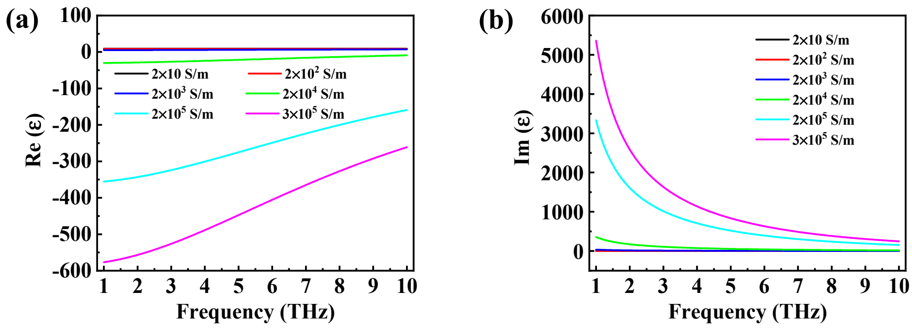

Figure 2. (**a**) The real and (**b**) imaginary parts of the VO_2 relative dielectric constant for different conductivities.

Absorptivity is a crucial parameter for evaluating absorber performance and can be expressed as A(ω) = 1 − R(ω) − T(ω), where T(ω) is the transmission coefficient and R(ω) is the reflection coefficient. Owing to the thickness of the metal film being greater than the penetration depth, T(ω) was close to zero within the operating frequency range. Therefore, A(ω) = 1 − R(ω) could be used to simplify the equation above. The absorption characteristics of this design were estimated by employing the commercial software CST 2018 on the basis of the FDTD method, where periodic boundary conditions are used in the x and y directions and Floquet ports are used in the z direction, and a plane wave was incident on the designed absorbers.

Although numerical simulation could be used to design the proposed device structure, the potential feasible preparation methods were worth exploring. Therefore, a potential fabrication method was proposed. First, a 200 nm thick metallic ground layer was deposited on a glass substrate by magnetron sputtering. A 9.5 μm thick dielectric layer is coated by spin coating. Then, a single layer of graphene was fabricated using chemical vapor deposition and a picosecond laser [33]. Next, 160 nm thick VO_2 was deposited on the graphene patterned by magnetron sputtering [34]. The ion gel was prepared by dissolving PVDF-HFP in acetone with the aid of a magnetic stirrer for an hour, before adding the EMIM TFSI into the solution and stirring for 24 h. The 100 nm thick ion gel was then spin-coated on the structure and dried in ambient conditions for one hour [35]. Using the above steps, the final sample could be prepared.

3. Results and Discussion

When the VO_2 was in the metal phase state with a conductivity of 3×10^5 S/m, the absorption spectra of the proposed broadband absorber were calculated and shown in Figure 3. The absorption bandwidth with an absorptivity of more than 90% was found to be 6.35 THz (2.30–8.65 THz). The absorption was very high, but it was not uniform. There were certain kinds of oscillation. The cause of these oscillations was graphene film interference. It was observed that two perfect absorption peaks were located at $f_1 = 5.36$ THz and $f_2 = 8.08$ THz.

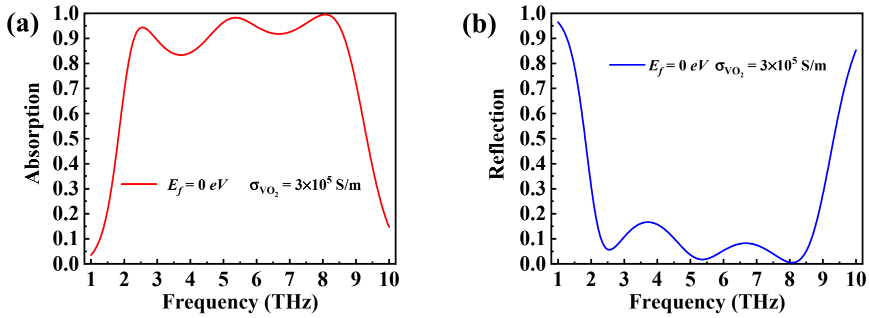

Figure 3. (**a**) Absorption and (**b**) reflection curves when $E_f = 0$ eV and $\sigma_{VO2} = 3 \times 10^5$ S/m.

Impedance matching, which explains that absorption tends to unity when the effective impedances of the free space and the absorber are matched, could also explain the absorption bandwidth of the metasurface absorber presented in this study. According to the impedance matching theory, the absorption of the absorber under normal incidence is as follows [36]:

$$A(\omega) = 1 - R(\omega) = 1 - \left|\frac{Z(\omega) - Z_0}{Z(\omega) + Z_0}\right|^2 = 1 - \left|\frac{Z_r(\omega) - 1}{Z_r(\omega) + 1}\right|^2 \quad (6)$$

where $Z_0 = \sqrt{\mu_0/\epsilon_0}$ and $Z(\omega) = \sqrt{\mu(\omega)/\epsilon(\omega)}$ are the effective impedances of the free space and the absorber, respectively, and $Z_r(\omega) = Z(\omega)/Z_0$ is the relative impedance between the absorber and the free space. The characterization of the metasurface absorber and the calculation of the relative impedance could be achieved using the scattering parameter inversion technique [23]:

$$Z_r(\omega) = \sqrt{\frac{(1 + S_{11}(\omega))^2 - S_{21}(\omega)^2}{(1 - S_{11}(\omega))^2 - S_{21}(\omega)^2}} \quad (7)$$

where S_{11} and S_{21} are scattering parameters, in which the first subscript represents the receiving port and the second subscript denotes the excitation port. The necessary condition for a metamaterial absorber to achieve perfect absorption is that the equivalent impedance of the metamaterial absorber matches the impedance of the free space, so that the incident electromagnetic wave enters the absorber to the maximum extent, and then the reflection reaches the minimum, so as to realize ultra-broadband absorption characteristics. The reflection is minimal and the absorption is close to the unit when the impedance of the absorber equals that of the free space or the equivalent relative impedance is equal to the unit ($Z_r = 1$). Figure 4 depicts the real and imaginary parts of the relative impedance. As the conductivity of VO_2 increased, the real part of Z_r inclined to 1, the imaginary part inclined to 0, and the absorption bandwidth became wider. When the conductivity of VO_2 was 3×10^5 S/m, the real part approached 1 and the imaginary part approached 0, which meant that the impedance of the proposed absorber almost matched that of the free space. At this time, the reflection of the absorber structure on the incident electromagnetic wave was almost zero, and the maximum loss of the incident terahertz wave was inside the insulation layer, achieving nearly perfect absorption.

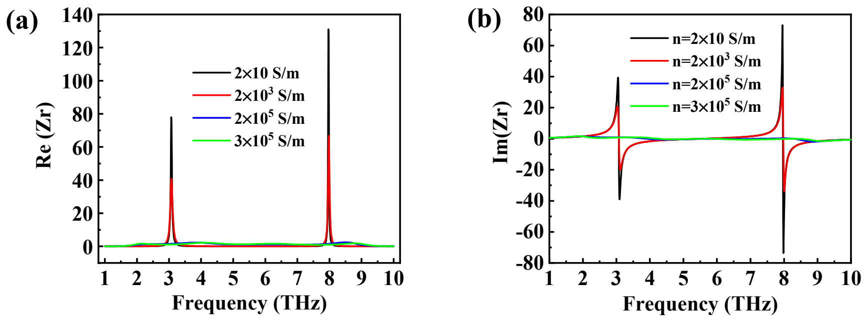

Figure 4. The (**a**) real part and (**b**) imaginary part of the relative impedance in broadband absorption.

In order to further explain the working mechanism of the broadband absorber, the electric field was investigated at frequencies of 2.55, 5.36, 7.83, and 8.08 THz, respectively, as illustrated in Figure 5. At the frequencies of 2.55, 5.36, 7.83, and 8.08 THz, the absorption of the absorbers was 94.4%, 98.2%, 98.6%, and 99.5%, respectively, and the absorption gradually increased. When the frequency equaled 2.55 and 5.36 THz, the electric field was concentrated between the four parts of the splitting ring, and the VO_2 resonance was formed between the left and right parts of the splitting rings. When the frequency equaled 7.83 and 8.08 THz, the electric field between the four parts of the splitting ring decreased, and the electric field at the edge of the splitting ring increased. It can be seen that the resonance at a low frequency was mainly caused by the electrical resonance between the parts of the VO_2 splitting ring, while the resonance at a high frequency was caused by the resonance of a single part of the VO_2 splitting ring.

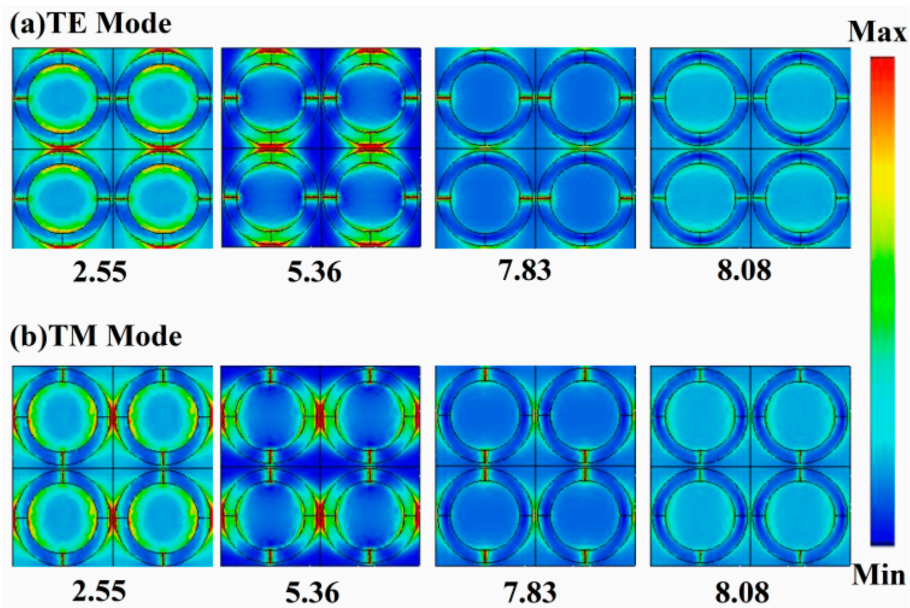

Figure 5. The simulated electric field intensity distributions of the proposed absorber at the frequencies of 2.55 THz, 5.36 THz, 7.83 THz, and 8.08 THz for (**a**) the TE mode and (**b**) the TM mode.

The absorption of this metasurface absorber could be dynamically regulated by adjusting the VO_2 conductivity from 2×10 S/m to 3×10^5 S/m. Figure 6 describes the VO_2 simulated absorption spectra with different electrical conductivity values under normal incidence and a graphene Fermi level of 0 eV, as well as the absorption spectra without graphene and with different graphene Fermi levels and a VO_2 conductivity of 3×10^5 S/m. Thus, the conductivity of VO_2 and the Fermi level of the graphene had an important effect on the designed absorption system performance, which offered a further degree of flexibility for the implementation of dynamically adjustable ultra-broadband absorbers.

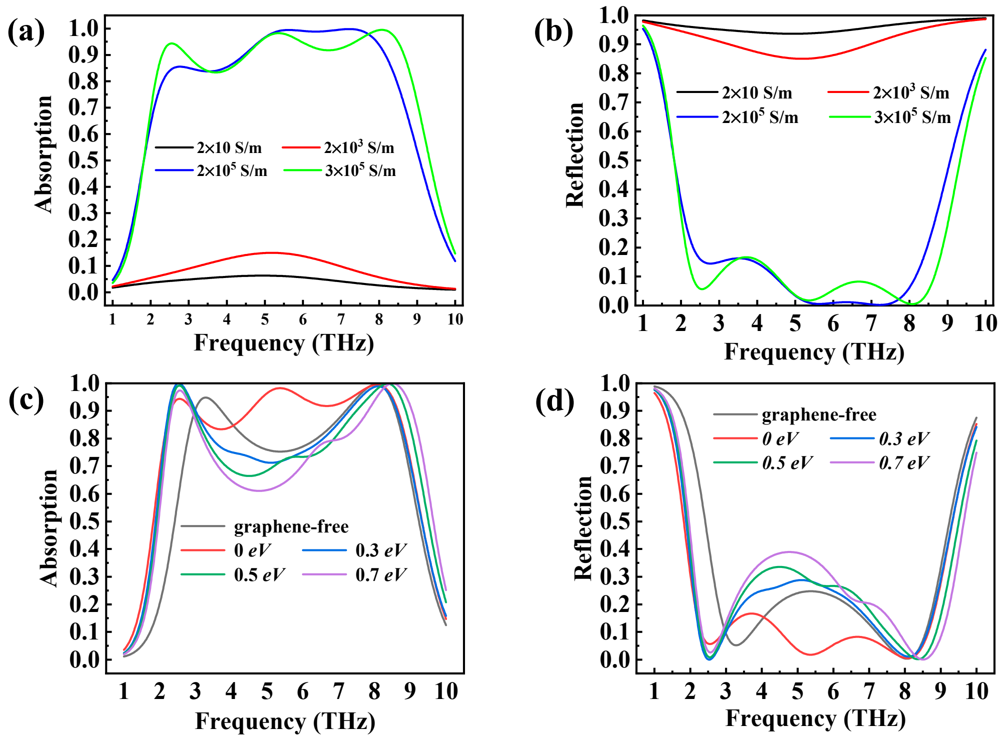

Figure 6. (**a**) Absorption spectra and (**b**) reflection spectra with different conductivities of VO_2 and a graphene Fermi level of 0 eV, (**c**) Absorption spectra and (**d**) reflection spectra without graphene, with different graphene Fermi levels, and with a VO_2 conductivity of 3×10^5 S/m.

Considering the possible fabrication errors of the metamaterial structure in the actual machining process, we studied in detail the impact of different geometrical parameters on the broadband absorptive properties. Except for the variable parameters, the parameters were fixed at the initial settings for this investigation. When the Fermi level of the graphene was E_f = 0 eV and the structural period was 20 μm, the operating frequency and intensity of the broadband and narrowband absorbance could be adjusted by the parameters. Figure 7 depicts the influence of the parameters (such as T_1, T_3, R_1, R_2, and g) on the absorption spectrum of the design metasurface absorber.

As shown in Figure 7a, when T_1 increased from 8.5 μm to 11.5 μm, a remarkable red shift could be observed at a high frequency such that the relative bandwidth reduced. In order to account for this red-shift phenomenon, the propagation phase (φ_p) could be employed, which is denoted by [37]:

$$f = \frac{c\varphi_p}{4T_1\sqrt{\varepsilon_r - \sin^2\alpha}} \tag{8}$$

where T_1, f, ε_r, c, and α are the thickness of insulator layer, the resonance frequency, the permittivity of the insulator layer, the speed of light in free space, and the incident angle, respectively. In this design, the parameters $\varepsilon_r = 1.96$ and $\alpha = 0°$. φ_p were considered to be fixed as well. The incident wave was a plane wave, φ_p. It is known that Equation (8) shows an inverse relationship between the resonant frequency and the thickness of the insulator layer. Therefore, the resonance frequency was red-shifted as parameter T_1 increased.

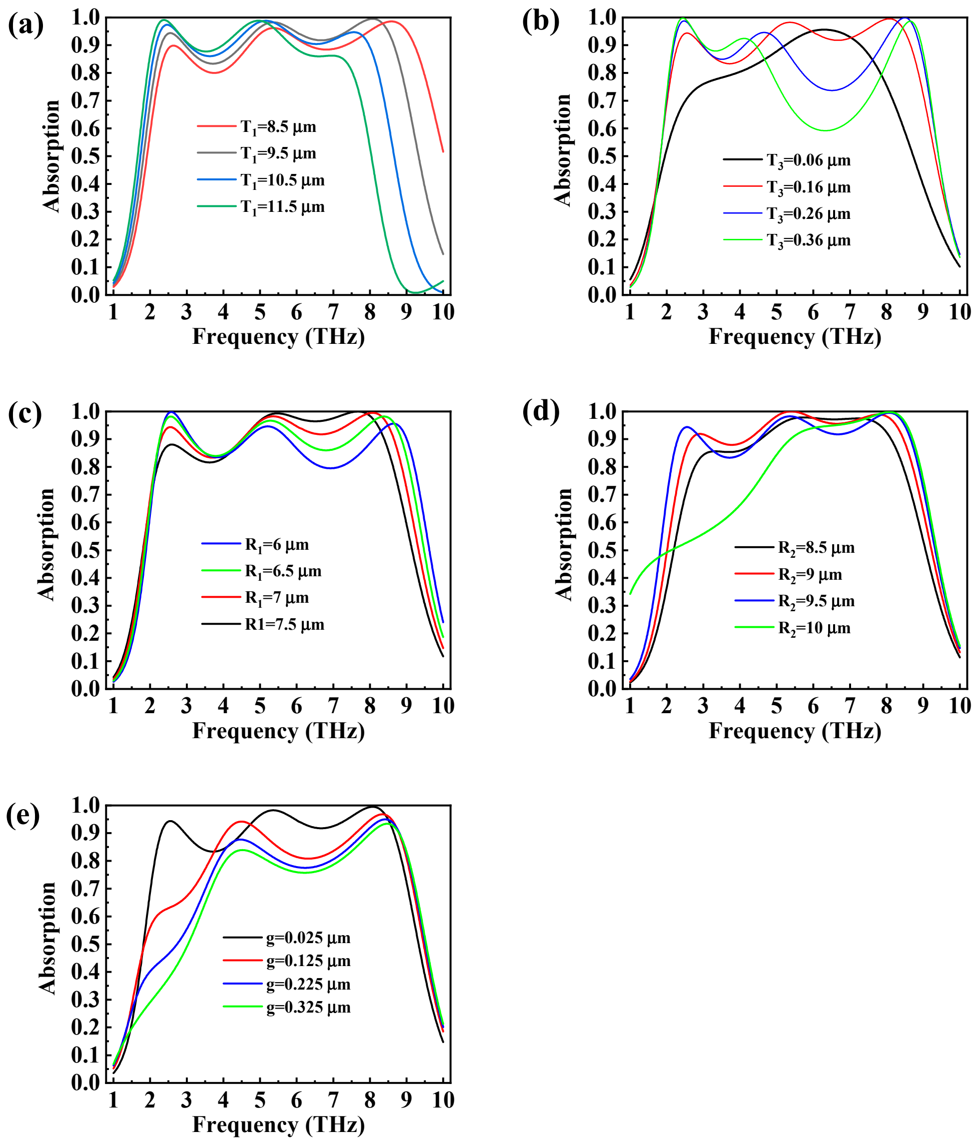

Figure 7. The absorption spectra of the absorber with distinct geometric parameters (**a**) T_1, (**b**) T_3, (**c**) R_1, (**d**) R_2, and (**e**) g under a normal TE incident wave.

The absorption spectra of the designed absorber with different thicknesses of the bottom layer are depicted in Figure 7b. When the thickness T_3 was equal to 0.16 µm, the ultra-broadband and quasi-perfect absorption of the designed absorber was achieved. Therefore, the thickness of T_3 = 0.16 µm was selected as the optimal geometric parameter. Figure 7c,d depict the absorption performance of the absorber with ring radius R_1 and R_2, respectively. When the radius R_1 varied from 6 to 7.5 µm, there was a significant red shift in the high-frequency absorption. On the contrary, as the radius R_2 increased from 8.5 to 10 µm, the absorption performance at a low frequency had a remarkable red shift. The LC circuit model could be utilized to elucidate the resonant frequency of the proposed absorber, which is expressed as [37]:

$$\mathrm{f} = \frac{1}{2\pi\sqrt{\mathrm{LC}/2}} \propto \frac{1}{\mathrm{R}} \tag{9}$$

where R, C, and L, are the radius, the total capacitance, and the inductance of the ring, respectively. It can be observed that the frequency in this equation has an inverse relationship with the ring radius. Thus, as the radius of the ring increased, the peak of the absorption moved towards a low frequency.

In Figure 7e, as the gap of the splitting ring increased, the absorption between the two resonant frequencies, shifting from 5 THz to 8.65 THz, decreased significantly. Furthermore, the absorption peak at 2.3 THz reduced with an increase in parameter g. However, the bandwidth showed no distinct change. Based on the above considerations, we finally selected the size of the broadband absorber as T_1 = 9.5 μm, T_2 = 0.2 μm, T_3 = 0.16 μm, R_1 = 7 μm, R_2 = 9.5 μm, and g = 0.025 μm.

In practical applications, it is crucial that the absorber be insensitive to the polarization angle. To investigate the absorption effect of the absorber under oblique incidence, broadband absorption spectra with polarization angles of 0° to 90°, incidence angles of 0° to 90°, and a step size of 10° were simulated in the frequency range from 1 to 10 THz. Figure 8a,b depict the absorption spectra of electromagnetic waves that were incident in the normal direction and had different polarization angles for TM and TE modes. It is clear that the absorption at each frequency point experienced no shift with the change in polarization angle. This polarization-insensitive characterization might have been a result of the symmetrical structure of the designed absorber.

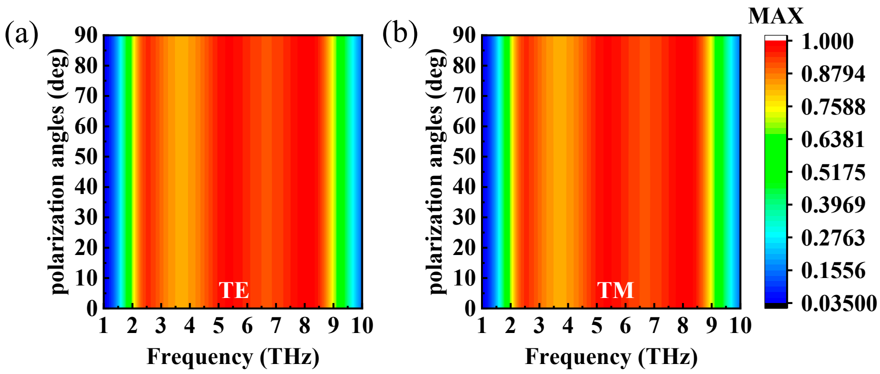

Figure 8. The absorption spectra of the designed absorbers with different polarization angles for (**a**) TE mode and (**b**) TM mode.

Figure 9a shows the absorption spectra with various incidence angles for the TE-polarized incident wave. The absorption decreased in the low- and high-frequency absorption bands with the increased incident angle, but a maximum absorption coefficient of 89% could still be achieved at the incident angle of 70°. Figure 9b shows the absorption spectra with various incidence angles for the TM-polarized incident wave. An absorption intensity over 90% could also be obtained until the incident angle rose to 60°. But the absorption bandwidth was greatly affected by the incident angle, since the tangential component of the electric field parallel to the x axis of the TM-polarized incident wave decreased with the increase in the angle of incidence. In addition, both polarization situations showed a blue shift with a rising incidence angle, which was caused by the parasitic resonance on the absorber surface at high incidence angles [38].

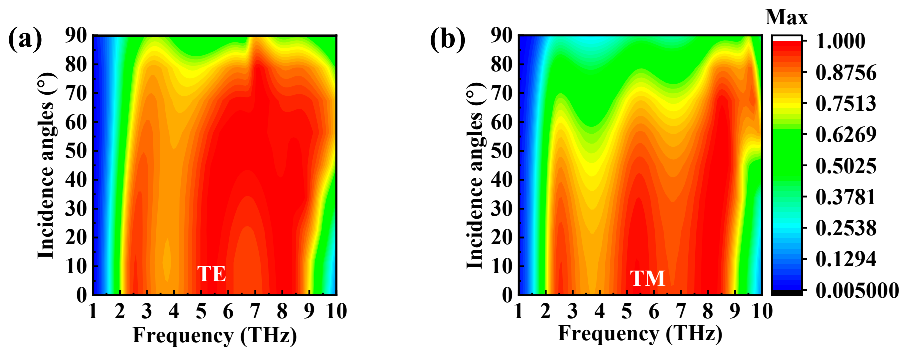

Figure 9. The absorption spectra of the designed absorbers with different incident angles for (**a**) TE mode and (**b**) TM mode.

Terahertz metamaterial absorbers based on VO_2 and graphene have attracted more and more attention. To illustrate the advantages of the absorbers designed in this paper, we compared their broadband absorption characteristics with those of other published papers in Table 1. The design of the absorber layer number, broadband performance, and adjustable range had good performance.

Table 1. Comparison of broadband absorption performance between different absorbers.

References	Constitutive Materials	Number of Layers	Absorption Bandwidth (THz)	Angular Stability	Polarization Insensitive
[39]	Graphene and VO_2	7	1.6 (0.8–2.4)	55	Yes
[40]	Graphene and VO_2	6	1.3 (1.05–2.35)	50	Yes
[41]	VO_2	3	3.3 (2.34–5.64)	55	Yes
[42]	Graphene and VO_2	3	1.03 (1–2.03)	50	No
This work	Graphene and VO_2	4	6.35 (2.30–8.65)	50	Yes

4. Conclusions

In summary, we designed a broadband tunable THz metamaterial absorber using VO_2 and graphene that could achieve switching performance with nearly perfect broadband absorption. It was demonstrated that the proposed broadband absorber could achieve nearly perfect absorption from 2.30 to 8.65 THz in both numerical simulations and theoretical calculations. In addition, the proposed broadband absorber could be flexibly adjustable, and the absorption amplitude could be continuously increased from 6% to 99% by changing the conductivity of VO_2. Due to absorbing devices having a tuning range width and polarization insensitivity, etc., they have good application prospects in such areas as tunable filters, sensors, and switches.

Author Contributions: Conceptualization, L.Z. and R.F.; data curation, L.Z.; formal analysis, H.S.; funding acquisition, R.F. and L.Z.; investigation, X.L.; methodology, L.Z. and R.F.; resources, H.S.; software, L.Z.; supervision, R.F.; validation, R.F.; visualization, H.S.; writing—original draft, L.Z. and R.F.; writing—review and editing, H.S. and X.L. All authors have read and agreed to the published version of the manuscript.

Funding: This work was partially supported by the Key Research and Development Plan of Shanxi Province (202102030201005), the Natural Science Foundation of Shanxi Province (202203021222070), Shanxi Scholarship Council of China, and Scientific and Technologial Innovation Programs of Higher Education Institutions in Shanxi (No. 2022L528).

Data Availability Statement: The data that support the findings of this study are available from the corresponding author upon reasonable request.

Acknowledgments: Thank you very much for the support of the Key Laboratory of Micro/nano Devices and Systems, Ministry of Education of the North University of China.

Conflicts of Interest: The authors declare no conflict of interest.

References

1. Luo, H.; Cheng, Y. Thermally tunable terahertz metasurface absorber based on all dielectric indium antimonide resonator structure. *Opt. Mater.* **2020**, *102*, 109801. [CrossRef]
2. Han, X.; Xiao, D.M.; Zhang, H. Wave-thermal effect of a temperature-tunable terahertz absorber. *Opt. Express* **2021**, *29*, 38557.
3. Shah, A.R.; Naveed, M.A.; Ijaz, S.; Rahim, A.A.; Zubair, M.; Massoud, Y.; Mehmood, M.Q. A functionality switchable meta-device: From perfect reflection to perfect absorption. *Phys. Scr.* **2023**, *98*, 095514. [CrossRef]
4. Zakir, S.; Bilal, R.M.H.; Naveed, M.A.; Baqir, A.; Khan, M.U.A.; Ali, M.M.; Saeed, M.A.; Mehmood, M.Q.; Massoud, Y. Polarization-Insensitive, Broadband, and Tunable Terahertz Absorber Using Slotted-Square Graphene Meta-Rings. *IEEE Photonics J.* **2023**, *15*, 4600108. [CrossRef]
5. Landy, N.I.; Sajuyigbe, S.; Mock, J.J.; Smith, D.R.; Padilla, W.J. Perfect Metamaterial Absorber. *Phys. Rev. Lett.* **2008**, *100*, 279–282. [CrossRef] [PubMed]
6. Long, Y.; Shen, L.; Xu, H.; Deng, H.; Li, Y. Achieving ultranarrow graphene perfect absorbers by exciting guided-mode resonance of one-dimensional photonic crystals. *Sci. Rep.* **2016**, *6*, 32312. [CrossRef]
7. Wen, Q.Y.; Zhang, H.W.; Xie, Y.S.; Yang, Q.H.; Liu, Y.L. Dual band terahertz metamaterial absorber: Design, fabrication, and characterization. *Appl. Phys. Lett.* **2009**, *95*, 207402. [CrossRef]

8. Li, M.; Liang, C.; Zhang, Y.; Yi, Z.; Chen, X.; Zhou, Z.; Yang, H.; Tang, Y.; Yi, Y. Terahertz wideband perfect absorber based on open loop with cross nested structure—Sciencedirect. *Results Phys.* **2019**, *15*, 102600–102603. [CrossRef]
9. Hu, D.; Wang, H.Y.; Zhu, Q.F. Design of six-band terahertz perfect absorber using a simple U-shaped closed-ring resonator. *IEEE Photonics J.* **2016**, *8*, 1–8. [CrossRef]
10. Bao, Z.Y.; Wang, J.C.; Hu, Z.D. Coordinated multi-band angle insensitive selection absorber based on graphene metamaterials. *Opt. Express* **2019**, *27*, 31435–31445. [CrossRef] [PubMed]
11. Sun, P.; Zhou, C.; Jia, W.; Wang, J.; Xiang, C.; Xie, Y.; Zhao, D. Narrowband absorber based on magnetic dipole resonances in two-dimensional metal–dielectric grating for sensing. *Opt. Commun.* **2020**, *459*, 12946. [CrossRef]
12. Huang, L.; Chowdhury, D.R. Experimental demonstration of terahertz metamaterial absorbers with a broad and flat high absorption band. *Opt. Lett.* **2012**, *37*, 154. [CrossRef]
13. Cai, Y.J.; Xu, K.D. Tunable broadband terahertz absorber based on multilayer graphene-sandwiched plasmonic structure. *Opt. Express* **2018**, *26*, 31693–31705. [CrossRef] [PubMed]
14. Li, H.; Yu, J. Bifunctional terahertz absorber with a tunable and switchable property between broadband and dual-band. *Opt. Express* **2020**, *28*, 25225–25237. [CrossRef]
15. Kepi, P.; Ligmajer, F.; Hrtoň, M.; Ren, H.; Menezes, L.D.S.; Maier, S.A.; Šikola, T. Optically tunable mie-resonance VO_2 nanoantennas for metasurfaces in the visible. *ACS Photonics* **2021**, *8*, 1048–1057. [CrossRef]
16. Lei, L.; Lou, F.; Tao, K.; Huang, H.; Cheng, X.; Xu, P. Tunable and scalable broadband metamaterial absorber involving VO_2-based phase transition. *Photonics Res.* **2019**, *7*, 734–741. [CrossRef]
17. He, J.; Zhang, M.; Shu, S.; Yan, Y.; Wang, M. VO_2 based dynamic tunable absorber and its application in switchable control and real-time color display in the visible region. *Opt. Express* **2020**, *28*, 37590–37599. [CrossRef]
18. Chen, S.Q.; Cheng, H.; Yang, H.F. Polarization insensitive and omnidirectional broadband near perfect planar metamaterial absorber in the near infrared regime. *Appl. Phys. Lett.* **2011**, *99*, 253104. [CrossRef]
19. Zhang, Y.B.; Liu, W.W.; Li, Z.C. Ultrathin polarization-insensitive wide-angle broadband near-perfect absorber in the visible regime based on few-layer MoS_2 films. *Appl. Phys. Lett.* **2017**, *111*, 111109. [CrossRef]
20. Zhao, Y.T.; Wu, B.; Huang, B.J. Switchable broadband terahertz absorber/reflector enabled by hybrid graphene-gold metasurface. *Opt. Express* **2017**, *25*, 7161–7169. [CrossRef] [PubMed]
21. Xiong, H.; Wu, Y.B.; Dong, J.M.; Tang, M.-C.; Jiang, Y.-N.; Zeng, X.-P. Ultra-thin and broadband tunable metamaterial graphene absorber. *Optic Express* **2018**, *26*, 1681–1688. [CrossRef]
22. Wang, Y.; Song, M.; Pu, M.; Gu, Y.; Hu, C.; Zhao, Z.; Wang, C.; Yu, H.; Luo, X. Luo. Staked graphene for tunable terahertz absorber with customized bandwidth. *Plasmonics* **2016**, *11*, 1201–1206. [CrossRef]
23. Smith, D.R.; Vier, D.C.; Koschny, T. Electromagnetic parameter retrieval from inhomogeneous metamaterials. *Phys. Rev. E* **2005**, *71*, 036617. [CrossRef]
24. Mou, N.L.; Sun, S.L.; Dong, H.X.; Dong, S.H.; He, Q.; Zhou, L.; Zhang, L. Hybridization-induced broadband terahertz wave absorption with graphene metasurfaces. *Opt. Express* **2018**, *26*, 11728–11736. [CrossRef]
25. Sun, P.; You, C.; Mahigir, A.; Liu, T.; Xia, F.; Kong, W.; Veronis, G.; Dowling, J.P.; Dong, L.; Yun, M. Graphene-based dual-band independently tunable infrared absorber. *Nanoscale* **2018**, *10*, 15564–15570. [CrossRef]
26. Hanson, G.W. Dyadic Green's functions and guided surface waves for a surface conductivity model of graphene. *J. Appl. Phys.* **2008**, *103*, 064302. [CrossRef]
27. Hu, N.; Wu, F.L.; Bian, L.A. Dual broadband absorber based on graphene metamaterial in the terahertz range. *Opt. Mater. Express* **2018**, *8*, 3899. [CrossRef]
28. Liu, M.; Yin, X.B. A graphene-based broadband optical modulator. *Nature* **2011**, *474*, 64–67. [CrossRef]
29. Wang, S.X.; Kang, L.; Werner, D.H. Hybrid resonators and highly tunable terahertz metamaterials enabled by vanadium dioxide (VO_2). *Sci. Rep.* **2017**, *7*, 4326. [CrossRef]
30. Tian, X.M.; Li, Z.Y. An optically-triggered switchable mid-infrared perfect absorber based on phase-change material of vanadium dioxide. *Plasmonics* **2018**, *13*, 1393–1402. [CrossRef]
31. Ruzmetov, D.; Gopalakrishnan, G.; Deng, J. Electrical triggering of metal-insulator transition in nanoscale vanadium oxide junctions. *J. Appl. Phys.* **2009**, *106*, 083702. [CrossRef]
32. Wen, Q.Y.; Zhang, H.W.; Yang, Q.H. Terahertz metamaterials with VO_2 cut-wires for thermal tunability. *Appl. Phys. Lett.* **2010**, *97*, 021111. [CrossRef]
33. Lin, Z.; Ye, X.; Han, J.; Chen, Q.; Fan, P.; Zhang, H.; Xie, D.; Zhu, H.; Zhong, M. Precise control of the number of layers of graphene by picosecond laser thinning. *Sci. Rep.* **2015**, *5*, 11662. [CrossRef] [PubMed]
34. Yue, Y.; Chen, Y.; Wang, S.; Zhang, N.; Li, A.; Yang, H. A simple method for the preparation of patterned graphene electrodes and its application in organic lightemitting diodes array. *Mater. Lett.* **2019**, *251*, 152–155. [CrossRef]
35. Meng, K.; Park, S.J.; Li, L.H.; Bacon, D.R.; Chen, L.; Chae, K.; Park, J.Y.; Burnett, A.D.; Linfield, E.H.; Davies, A.G.; et al. Tunable broadband terahertz polarizer using graphene-metal hybrid metasurface. *Opt. Express* **2019**, *27*, 33769–33779. [CrossRef]
36. Watts, C.M.; Liu, X.; Padilla, W.J. Metamaterial electromagnetic wave absorbers. *Adv. Mater.* **2012**, *24*, OP98–OP120. [CrossRef]
37. Pan, W.; Yu, X.; JZhang Zeng, W. A broadband terahertz metamaterial absorber based on two circular split rings. *IEEE J. Quantum Electron.* **2018**, *53*, 8500206. [CrossRef]

38. Zhu, J.; Li, C.; Ou, J.-Y.; Liu, Q.H. Perfect light absorption in graphene by two unpatterned dielectric layers and potential applications. *Carbon* **2019**, *142*, 430–437. [CrossRef]
39. Wang, G.; Wu, T.; Jiang, J.; Jia, Y.; Gao, Y.; Gao, Y. Switchable terahertz absorber from single broadband to triple-narrowband. *Diam. Relat. Mater.* **2022**, *130*, 109460. [CrossRef]
40. Liu, Y.; Huang, R.; Ouyang, Z. Terahertz absorber with dynamically switchable dual-broadband based on hybrid metamaterial with vanadium dioxide and graphene. *Opt. Express* **2021**, *29*, 13. [CrossRef]
41. Badri, S.H.; Gilarlue, M.M.; Saeidnahaei, S.; Kim, J.S. Narrowband-to-broadband switchable and polarization-insensitive terahertz metasurface absorber enabled by phase-change material. *J. Opt.* **2022**, *24*, 025101. [CrossRef]
42. Zhou, R.; Jiang, T.; Peng, Z.; Li, Z.; Zhang, M.; Wang, S.; Li, L.; Liang, H.; Ruan, S.; Su, H. Tunable broadband terahertz absorber based on graphene metamaterials and VO_2. *Opt. Mater.* **2021**, *114*, 110915. [CrossRef]